

This is the author's final, peer-reviewed manuscript as accepted for publication (AAM). The version presented here may differ from the published version, or version of record, available through the publisher's website. This version does not track changes, errata, or withdrawals on the publisher's site.

# A study of Ar-N<sub>2</sub> supercritical mixtures using neutron scattering, molecular dynamics simulations and quantum mechanical scattering calculations

Alan K. Soper, Ioannis Skarmoutsos, Jacek Kłos,  
Jannis Samios, Sarantos Marinakis

## Published version information

**Citation:** AK Soper et al. 'A study of Ar-N<sub>2</sub> supercritical mixtures using neutron scattering, molecular dynamics simulations and quantum mechanical scattering calculations.' *Journal of Molecular Liquids*, vol. 290 (2019): 111168.

**DOI:** [10.1016/j.molliq.2019.111168](https://doi.org/10.1016/j.molliq.2019.111168)

©2019. This manuscript version is made available under the [CC-BY-NC-ND](https://creativecommons.org/licenses/by-nc-nd/4.0/) 4.0 Licence.

This version is made available in accordance with publisher policies. Please cite only the published version using the reference above. This is the citation assigned by the publisher at the time of issuing the AAM. Please check the publisher's website for any updates.

This item was retrieved from **ePubs**, the Open Access archive of the Science and Technology Facilities Council, UK. Please contact [epubs@stfc.ac.uk](mailto:epubs@stfc.ac.uk) or go to <http://epubs.stfc.ac.uk/> for further information and policies.



# A study of Ar-N<sub>2</sub> supercritical mixtures using neutron scattering, molecular dynamics simulations and quantum mechanical scattering calculations

Alan K. Soper<sup>a</sup>, Ioannis Skarmoutsos<sup>b</sup>, Jacek Kłos<sup>c</sup>, Jannis Samios<sup>d</sup>, Sarantos Marinakis<sup>e, f, \*</sup>

<sup>a</sup> ISIS Facility, STFC Rutherford Appleton Laboratory, Harwell Campus, Didcot Oxon OX11 0QX, UK

<sup>b</sup> Institute Charles Gerhardt Montpellier, UMR 5253 CNRS, Université de Montpellier, Place E. Bataillon Montpellier Cedex 05, 34095, France

<sup>c</sup> Department of Chemistry and Biochemistry, University of Maryland, College Park, MD 20742, USA

<sup>d</sup> National and Kapodistrian University of Athens, Department of Chemistry, Laboratory of Physical Chemistry, Panepistimiopolis, Athens 157-71, Greece

<sup>e</sup> School of Health, Sport and Bioscience, University of East London, Stratford Campus, Water Lane, London E15 4LZ, UK

<sup>f</sup> Department of Chemistry and Biochemistry, School of Biological and Chemical Sciences, Queen Mary University of London, Joseph Priestley Building, Mile End Road, London E1 4NS, UK

## ARTICLE INFO

### Article history:

Received 20 February 2019

Received in revised form 17 May 2019

Accepted 10 June 2019

Available online xxx

### Keywords:

Supercritical

Argon

Nitrogen

Neutron scattering

Molecular dynamics

Ar-N<sub>2</sub>

Supercritical mixture

## ABSTRACT

The microscopic structure of Ar-N<sub>2</sub> supercritical mixtures was obtained using neutron scattering experiments at temperatures between 128.4 and 154.1 K, pressures between 48.7 and 97.8 bar and various mole fractions. Molecular Dynamics simulations (MD) were used to study the thermodynamics, microscopic structure and single molecule dynamics at the same conditions. The agreement between experimental and theoretical results on the intermolecular structure was very good. Furthermore, a new explicitly-correlated coupled cluster potential energy surface was obtained for the Ar-N<sub>2</sub> van der Waals complex. The *ab initio* potential energy surface (PES) was found in agreement with the MD interaction potential. The global minimum of the *ab initio* PES  $D_e = 98.66 \text{ cm}^{-1}$  was located at the T-shaped geometry and at the intermolecular equilibrium distance of  $R_e = 7.00 a_0$ . The dissociation energy of the complex was determined to be  $D_0 = 76.86 \text{ cm}^{-1}$ . Quantum mechanical (QM) calculations on the newly obtained PES were used to provide the bound levels of the complex. Finally, integral and differential QM cross sections in Ar + N<sub>2</sub> collisions were calculated at collision energy corresponding to the average temperature of the experiments and at room temperature.

© 2019.

## 1. Introduction

Supercritical fluids have special properties that have led to a rich variety of applications including production of essential oils and pharmaceutical products, green chemistry, nuclear reactors and formation of nano- and micro-particles. Their special properties are closely related to some peculiar structural effects occurring in these fluids, which are absent in conventional phases such as liquid and gas. Supercritical fluids exhibit significant spatial density fluctuations, and these characteristic density inhomogeneities become even more pronounced close to the critical point of the fluid. Due to the close interrelation of the compressibility factor of a supercritical fluid with these density fluctuations, the presence of density inhomogeneities strongly affects the behaviour of the compressibility at these thermodynamic conditions, causing not only corresponding changes in their dissolving capability and reaction dynamics but also in the eclectic dissolution of different categories of solutes in supercritical solvents [1-3].

\* Corresponding author.

Email addresses: alan.soper@stfc.ac.uk (A.K. Soper); iskarmoutsos@hotmail.com (I. Skarmoutsos); jklos@umd.edu (J. Kłos); isamios@chem.uoa.gr (J. Samios); s.marinakis@uel.ac.uk (S. Marinakis)

Recent experimental and theoretical work [4-6] has also shown that structural transitions from liquid-like behaviour at high pressures to gas-like behaviour at low pressures may take place. Debenedetti and coworkers [7] have predicted that heavy-in-light near critical system will exhibit an enhancement of solute-solvent interactions, but the converse will be true for a light-in-heavy near critical system. The present work is the first joint systematic experimental and theoretical study of the effect of mass and concentration in the microscopic structure and molecular motion in binary supercritical mixtures.

The chosen binary system is the Ar-N<sub>2</sub>, where the molecular weights of Ar and N<sub>2</sub> are around 40 and 28 amu, respectively. Thus we will be able to contrast the behaviour between N<sub>2</sub> in-Ar (light-in-heavy) and Ar-in-N<sub>2</sub> (heavy-in-light) mixtures. The Ar-N<sub>2</sub> system has been studied extensively. Particularly relevant to our work here is a previous work on thermodynamics, potential energy surfaces (PES), and microscopic structure. The main results of pVT and VLE studies on Ar-N<sub>2</sub> have been critically summarized and reviewed elsewhere [8-12]. Many PES have been presented for this system with the most recent ones [13-17] based on *ab initio* calculations and sometimes refined using experimental data. However, most of the previous work on Ar-N<sub>2</sub> used a simple functional form to describe the intermolecular forces in the condensed phase. One of the reasons for that was that good classical models were already available for the pure components Ar and N<sub>2</sub>. Based on these models, one could use mixing

**Table 1**

$x_{N_2} - T_{\text{exp}} - P_{\text{exp}}$  state points employed in the neutron scattering measurements. The REFPROP [51] was used to calculate the density,  $\rho_{\text{REFPROP}}$ , and the  $Q=0$  limit of the structure factor,  $F(0) = (\rho k_B T \kappa_T - 1)$  Eq. (1) where  $\rho$  is the atomic number density and  $\kappa_T$  is the isothermal compressibility, corresponding to the experimental conditions, and the critical point ( $T_c$ ,  $P_c$ , and  $\rho_c$  (kg/m<sup>3</sup>)).

| $x_{N_2}$ | $T_{\text{exp}}$ | $P_{\text{exp}}$ | $\rho_{\text{REFPROP}}$ | $F(0)$ | $T_c$  | $P_c$ | $\rho_c$             |
|-----------|------------------|------------------|-------------------------|--------|--------|-------|----------------------|
|           | [K]              | [bar]            | [kg/m <sup>3</sup> ]    |        | [K]    | [bar] | [kg/m <sup>3</sup> ] |
| 0.00      | 154.1            | 48.9±0.5         | 288.29                  | 4.4    | 150.69 | 48.63 | 535.60               |
|           |                  |                  | 97.8±1.0                | 910.61 |        |       |                      |
| 0.25      | 147.7            | 48.9±0.5         | 342.63                  | 13.5   | 144.64 | 45.74 | 478.98               |
|           |                  |                  | 97.8±1.0                | 813.71 |        |       |                      |
| 0.50      | 141.2            | 48.7±0.4         | 488.95                  | 15.9   | 138.44 | 42.18 | 423.60               |
|           |                  |                  | 96.9±1.1                | 728.29 |        |       |                      |
| 0.75      | 134.8            | 48.9±0.1         | 509.84                  | 4.8    | 132.28 | 38.22 | 368.57               |
|           |                  |                  | 92.2±4.9                | 644.33 |        |       |                      |
| 1.00      | 128.4            | 49.4±0.6         | 484.62                  | 2.3    | 126.19 | 33.96 | 313.30               |
|           |                  |                  | 94.0±4.7                | 575.37 |        |       |                      |

rules for the interaction between Ar and N<sub>2</sub> to reproduce pVT and VLE experimental data.

Although the microscopic structure of the Ar-N<sub>2</sub> has not been studied in the past at the conditions of our experiments, we note the study by Danylchenko et al. [18] of Ar-N<sub>2</sub> clusters formed in isentropically expanding supersonic jets of Ar-N<sub>2</sub> mixtures at various pressures and compositions at 40 K. The amount of argon in the clusters was found to be always greater than its concentration in the gas phase. Also, for increasing Ar concentration, a transformation from the hexagonal close packed (hcp) to an hcp + fcc (face-centred cubic) structure was observed. The latter finding is similar to a previous study of the Ar-N<sub>2</sub> phase diagram by Barrett et al. [19] using x-ray diffraction. These authors found that the argon-rich solid solutions undergo a strain-induced transformation from hcp to fcc at low temperatures. Press et al. [20] used elastic and inelastic neutron scattering experiments to study solid solutions of Ar and N<sub>2</sub> and found that

adding Ar stabilizes a hexagonal disordered structure down to low temperatures without long-range orientational order. Langel [21] presented the librational spectrum of N<sub>2</sub> in Ar in matrix isolation at 7 K and the results compared well with molecular dynamics (MD) simulations, albeit at a much higher temperature of 79 K.

Despite the fact that previous work on the Ar-N<sub>2</sub> mixture is sparse, the pure components have been investigated using neutron and X-ray scattering and MD simulations. The structure factor and radial distribution function of liquid argon were originally measured by Yarnell et al. [22]. De Schepper et al. [23] performed inelastic neutron scattering experiments on liquid Ar and observed short-wavelength sound modes at 120 K and 2 MPa. The same authors explained these experimental data along with newly reported measurements at 11.5 and 40.0 MPa using mode coupling theory [24]. van Well et al. [25] obtained the coherent dynamic structure factor,  $S(k, \omega)$ , in the liquid phase at 120 K and pressures between 2 and 39 MPa. Fredrikze et al. [26] measured the static structure factor  $S(k)$  at 140 K and subcritical densities, and used their results to estimate the intermolecular potential. Bafile et al. [27] measured the neutron Brillouin scattering at subcritical densities of Ar at 302 K and pressures of 8 and 20 MPa. Their experimental results were in good agreement with extended hydrodynamic modes. Neutron Brillouin scattering in liquid Ar was obtained by Mos et al. [28] at temperatures between 120 and 141 K and pressures 20 and 43 MPa. It was shown that linearized hydrodynamics predicted a weaker damping in the propagating density fluctuations than the experimentally observed. Pfleiderer et al. (see [29] and references therein) investigated the structure in the supercritical phase at 350 K using neutron diffraction and ab initio molecular dynamics simulations. Their results as well as previous work in the liquid phase at 85 K showed that the agreement between theory and experiment was very good. Bomont et al. [30] used the self-integral equation method to calculate the structure and thermodynamic properties at the supercritical conditions employed by Pfleiderer et al. [29], and showed that there were only small differences between an empirical and an ab initio potential.

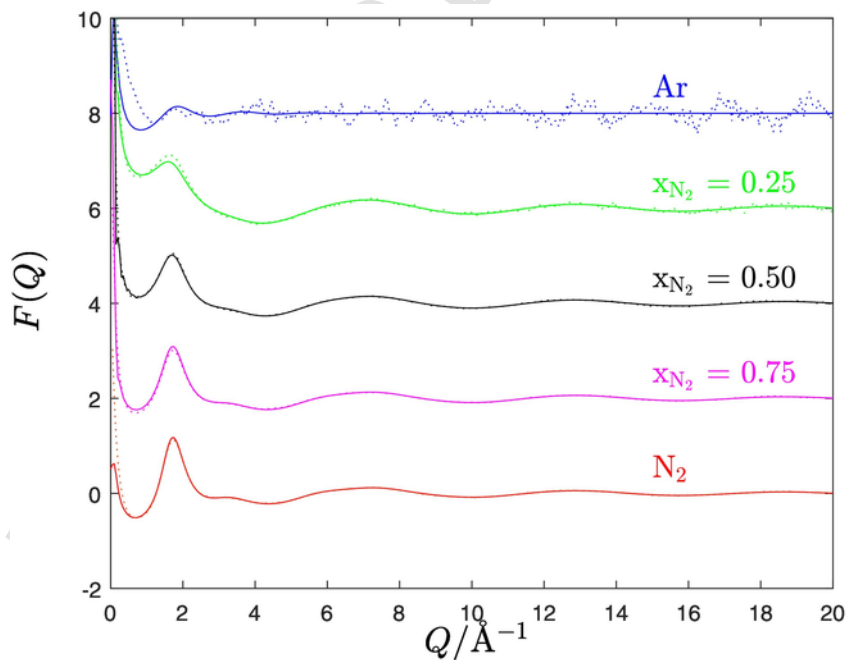


**Fig. 1.** Comparison between experimental weighted sum of the partial structure factors  $F(Q)$  (points), Eq. (1), for Ar-N<sub>2</sub> mixtures at around 49 bar with EPSR simulation results (lines) discussed in Section 2.1. The curves for lower  $x_{N_2}$  have been shifted along the y-axis by 2, 4, 6, and 8.

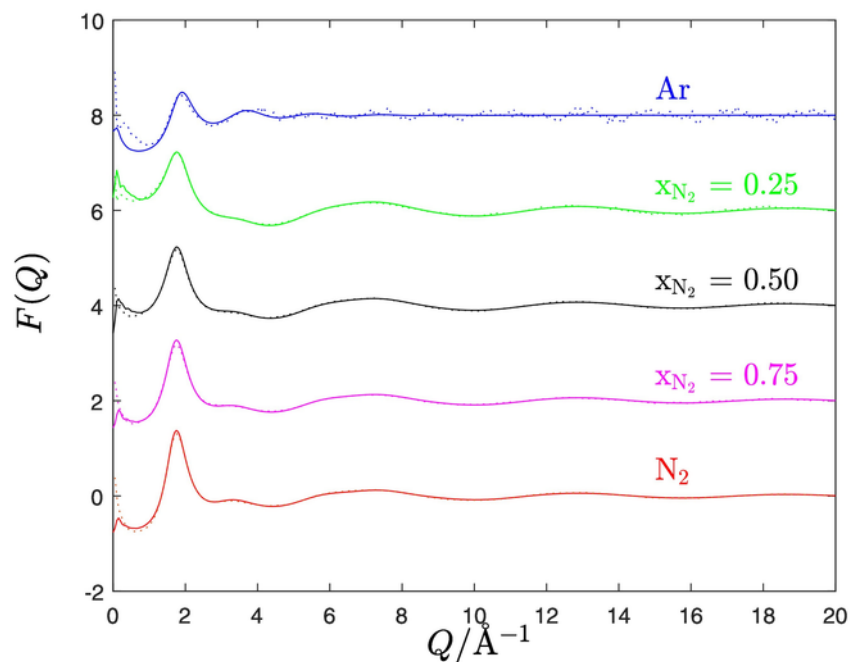


**Fig. 2.** Comparison between experimental weighted sum of the partial structure factors  $F(Q)$  (points), Eq. (1), for Ar-N<sub>2</sub> mixtures at pressures between 92 and 98 bar with EPSR simulation results (lines) discussed in Section 2.1. The curves for lower  $x_{N_2}$  have been shifted along the y-axis by 2, 4, 6, and 8.

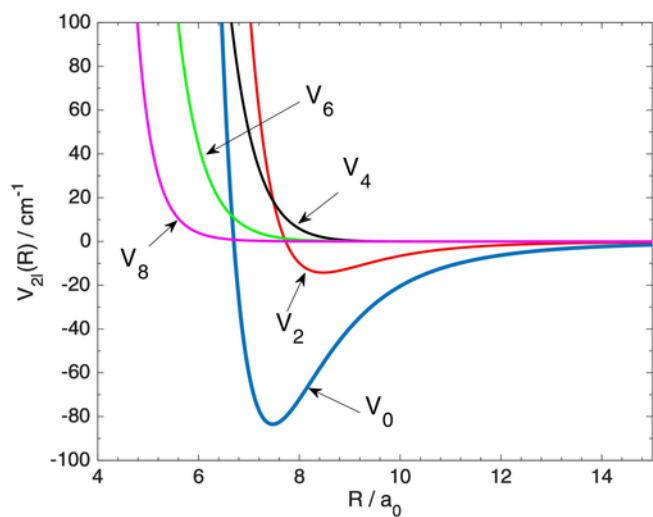


**Fig. 3.** The first five radial expansion coefficients (see Eq. (4)) of the Ar-N<sub>2</sub> CCSD(T)-F12a PES.

Regarding nitrogen in the condensed and gas phase, many studies have been performed to investigate its microscopic structure. For example in the solid phase, Powell et al. [31] used neutron scattering to study the  $\beta$ -phase at around 40K and at various pressures up to 120MPa. Sullivan and Egelstaff [32] obtained the structure factor at 296 and 300K and densities of between  $0.34$  and  $0.4 \times 10^{22}$  molecules  $\text{cm}^{-3}$  and the agreement of the experimental and theoretical data was not very good. In a later study, Sullivan and Egelstaff [33] obtained neutron scattering data at 160K and densities of between  $0.24$  and  $0.56 \times 10^{22}$  molecules  $\text{cm}^{-3}$  and reanalysed the previous data taking into account the inelasticity term. Overall, the agreement between theory and experiment was good but the available intermolecular potentials could not reproduce fully the data. Deraman et

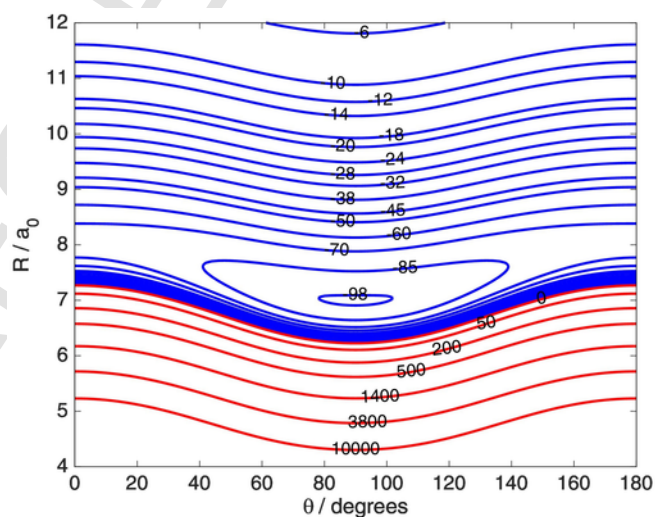


**Fig. 4.** Contour plot of the ab initio CCSD(T)-F12a PES for the Ar-N<sub>2</sub> van der Waals complex. Energy in units of  $\text{cm}^{-1}$ .

al. [34] measured neutron scattering at 294K and 100bar. Their experimental data were in best agreement with a site-site potential which included quadrupole moment. That potential was originally by Cheung and Powles [35] but the parameters were optimized by Deraman et al. resulting to a value of quadrupole moment around 20% higher than the experimental one. In the same year, Egelstaff et al. [36] investigated the structure and dynamics of dense nitrogen gas at temperatures around 296 K and at various densities up to 65% of the triple point density corresponding to pressures from 34 to 95 MPa. Egelstaff et al. [37] measured the neutron Brillouin scattering at room temperature and densities of  $5.82$  and  $9.05$  atoms  $\text{nm}^{-3}$  corresponding to pressures of 27 and 51 MPa. At those experimental conditions, a comparison between Navier-Stokes theoretical treat-

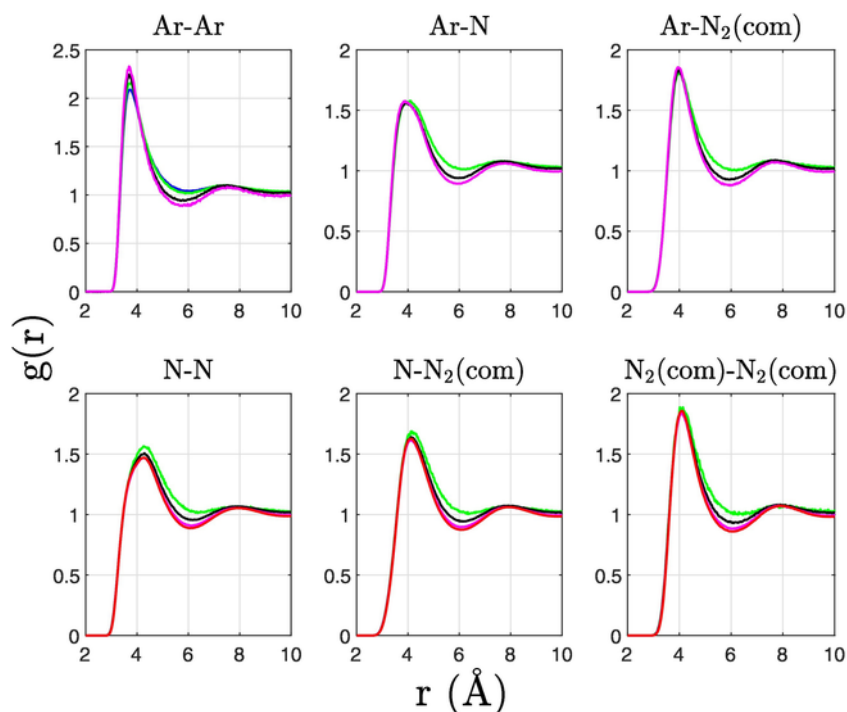


**Fig. 5.** Experimental pair radial distribution functions (RDF) for the Ar-Ar, Ar-N, Ar-N<sub>2</sub>(com), N-N, N-N<sub>2</sub>(com), and N<sub>2</sub>(com)-N<sub>2</sub>(com) separations of Ar-N<sub>2</sub> mixture at various values of N<sub>2</sub> mole fractions at around 49 bar: pure Ar (blue),  $x_{N_2} = 0.25$  (green),  $x_{N_2} = 0.50$  (black),  $x_{N_2} = 0.75$  (magenta), pure N<sub>2</sub> (red).

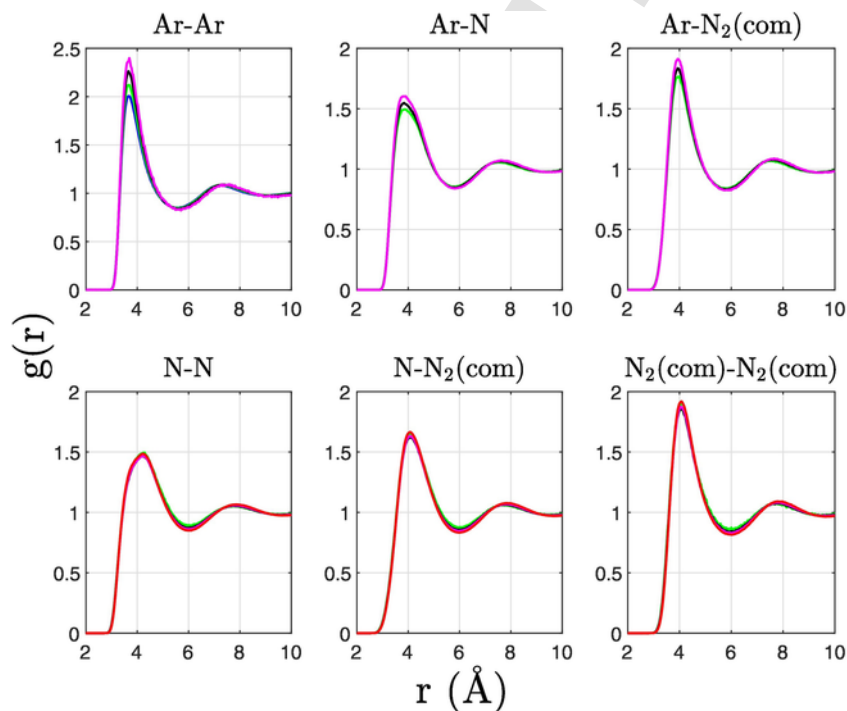


**Fig. 6.** Experimental pair radial distribution functions (RDF) for the Ar-Ar, Ar-N, Ar-N<sub>2</sub>(com), N-N, N-N<sub>2</sub>(com), and N<sub>2</sub>(com)-N<sub>2</sub>(com) separations of Ar-N<sub>2</sub> mixture at various values of N<sub>2</sub> mole fractions at pressures 92–98 bar: pure Ar (blue),  $x_{N_2} = 0.25$  (green),  $x_{N_2} = 0.50$  (black),  $x_{N_2} = 0.75$  (magenta), pure N<sub>2</sub> (red).

ment and generalized hydrodynamic calculations was possible. Youden et al. [38] measured the coherent scattering function,  $S(Q, \omega)$  as  $Q$  is increased away from the hydrodynamic region for N<sub>2</sub> at 295 K at pressures of 27.3 and 46.1 MPa, which correspond to densities of

0.9 and  $1.3\rho_c$ , respectively. Backx et al. [39] performed simulations for previous measurements of the dynamic structure factor. They showed that the agreement between the site-site plus quadrupole model of Cheung and Powles and experiment on the dynamic struc-

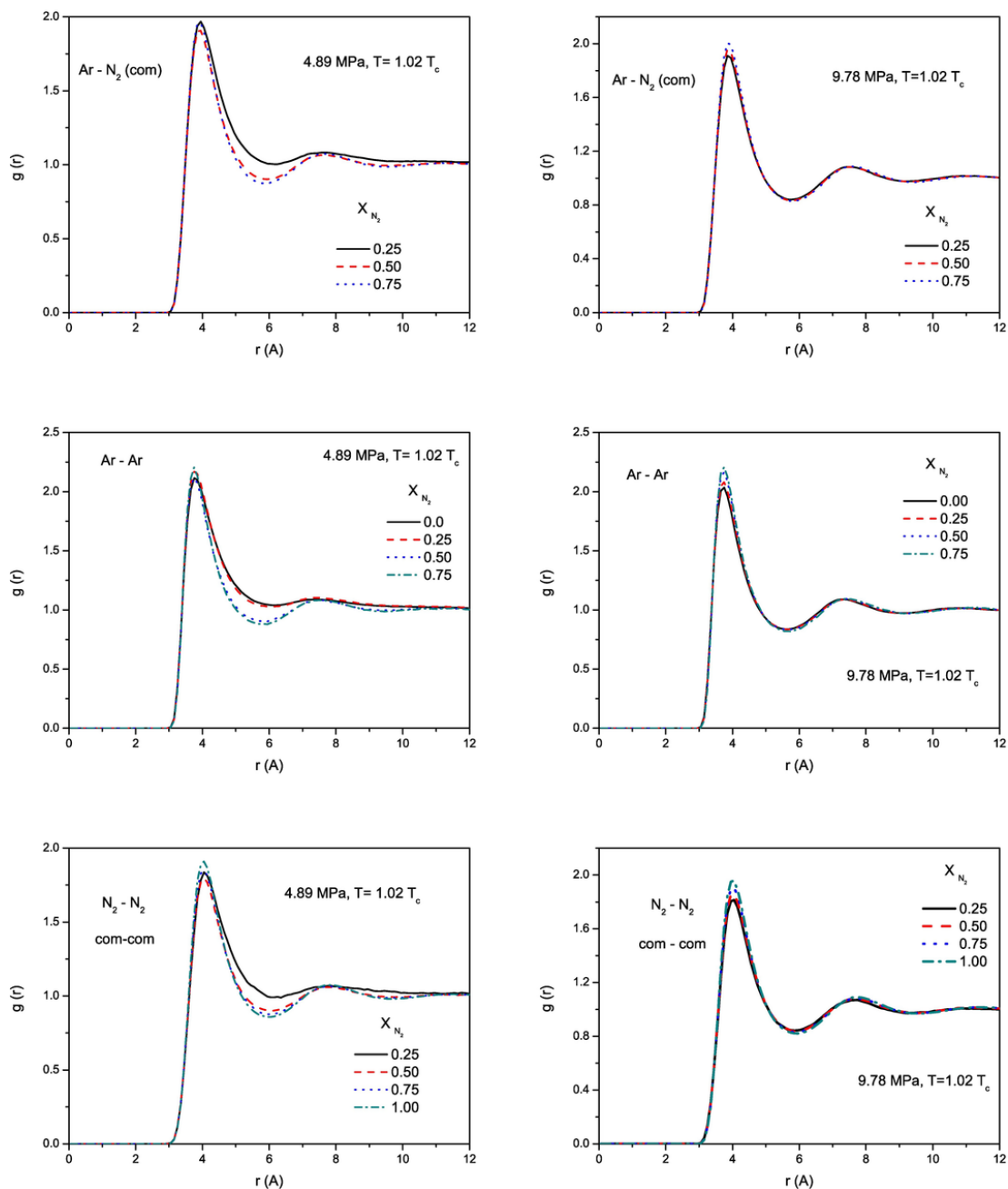


Fig. 7. MD RDF for the Ar-N<sub>2</sub>(com), Ar-Ar, and N<sub>2</sub>(com)-N<sub>2</sub>(com) pairs in Ar-N<sub>2</sub> mixtures at various compositions.

ture factor was worse than the agreement on the static structure factor, and suggested for improvements of the potential at short range. Potoff et al. [40] presented a non-polarizable all-atom transferable potential for phase equilibria (TraPPE) force field for N<sub>2</sub> which could reproduce the VLE experimental results. Recently, Strak et al. [41-43] used ab initio quantum mechanical calculations to obtain the intermolecular PES, and to perform MD calculations of the equation of state and shear viscosity. More recently, Ciocco et al. [44] derived two five-site potential energy function for N<sub>2</sub>, one including and one neglecting explicit induction effects, and used two differing sets of mixing rules. The proposed potential was efficient for solid, liquid, and gas phases. We also note that interaction-induced phe-

nomena, such as absorption in the infrared, have been studied extensively [45, 46].

The present study aims to provide a joint experimental and theoretical study of Ar-N<sub>2</sub> supercritical mixtures. The critical constants of natural N<sub>2</sub> are  $T_c = 126.19\text{K}$ ,  $\rho_c = 11.1\text{ mol/L}$ ,  $P_c = 33.978\text{ bar}$  [47], and of natural Ar are  $T_c = 150.86\text{K}$ ,  $\rho_c = 13.41\text{ mol/L}$ ,  $P_c = 4.8979\text{ bar}$  [47]. The experiments were performed at temperature  $T=1.02T_c$ , where  $T_c$  is the critical temperature of the mixture. The critical temperatures of the mixtures at the required mole fractions were predicted prior to experiments based on previous measurements by Jones and Rowlinson [48]. Because of the apparatus employed in ref. [48], the critical pressure of the Ar-N<sub>2</sub> mixture was not measured [49]. In order to avoid the critical pressure, where fluctuations

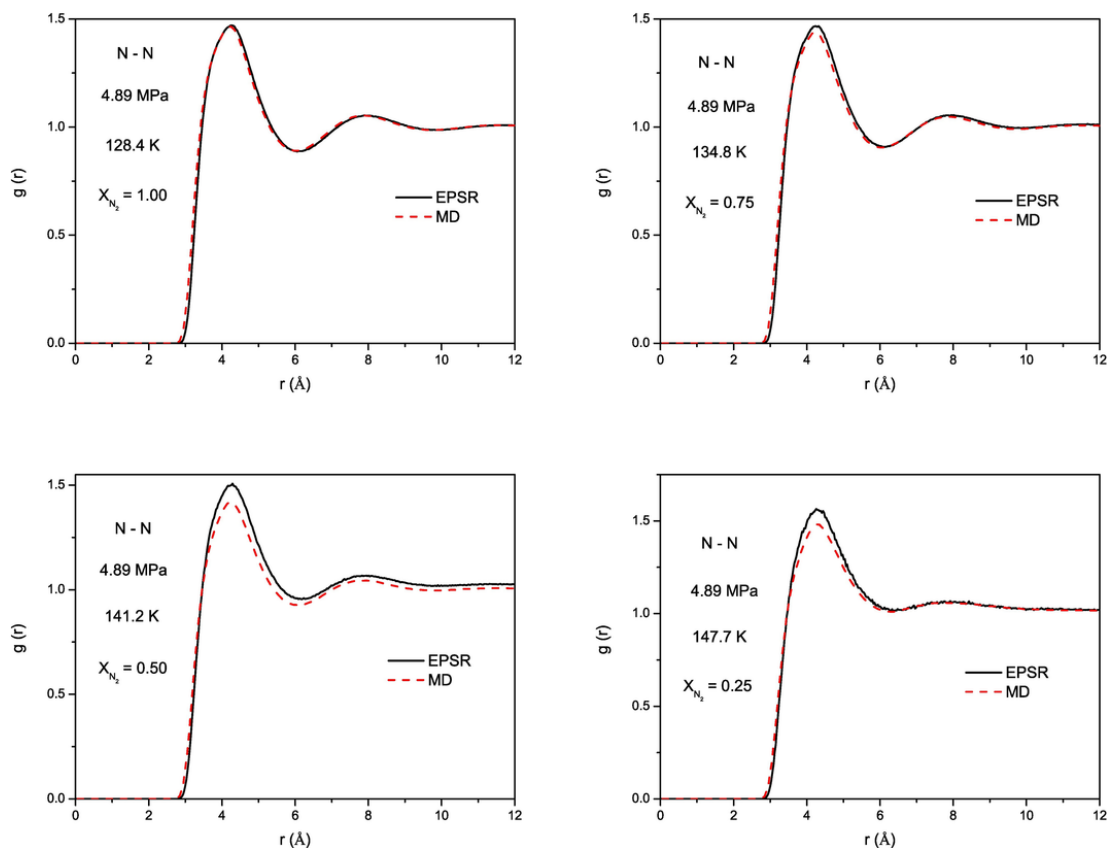


Fig. 8. Comparison between the EPSR and MD N-N RDF in Ar-N<sub>2</sub> mixtures at various compositions at pressure of 48.9 bar.

Table 2

Comparison between the MD results for the density,  $\rho_{MD}$  (g/cm<sup>3</sup>), at  $T=1.02T_c$  with predictions,  $\rho_{REFPROP}$  (g/cm<sup>3</sup>), using REFPROP [51] for the  $x_{N_2}-T_{exp}-P_{exp}$  state points employed in the neutron scattering measurements (Table 1). The coordination numbers were obtained using a cut-off of 5.95 Å corresponding to the first coordination shell.  $n_{Ar-N_2}$  corresponds to N<sub>2</sub> molecules in the coordination shell around Ar, and  $n_{N_2-Ar}$  corresponds to Ar atoms in the coordination shell around N<sub>2</sub>.

| $x_{N_2}$ | $P_{MD}$<br>(bar) | $\rho_{MD}$ | $\rho_{REFPROP}$ | $n_{Ar-Ar}$ | $n_{Ar-N_2}$ | $n_{N_2-N_2}$ | $n_{N_2-Ar}$ |
|-----------|-------------------|-------------|------------------|-------------|--------------|---------------|--------------|
| 0.00      | 48.9              | 0.2755      | 0.2883           | 4.20        | -            | -             | -            |
|           | 97.8              | 0.9223      | 0.9106           | 11.77       | -            | -             | -            |
| 0.25      | 48.9              | 0.3280      | 0.3426           | 4.02        | 1.30         | 1.24          | 3.89         |
|           | 97.8              | 0.8162      | 0.8137           | 8.51        | 2.82         | 2.76          | 8.46         |
| 0.50      | 48.9              | 0.5340      | 0.4890           | 4.29        | 4.21         | 4.11          | 4.21         |
|           | 97.8              | 0.7280      | 0.7283           | 5.56        | 5.50         | 5.45          | 5.50         |
| 0.75      | 48.9              | 0.5280      | 0.5098           | 2.30        | 6.78         | 6.67          | 2.26         |
|           | 97.8              | 0.6479      | 0.6443           | 2.70        | 8.13         | 8.03          | 2.71         |
| 1.00      | 48.9              | 0.4921      | 0.4846           | -           | -            | 9.21          | -            |
|           | 97.8              | 0.5767      | 0.5754           | -           | -            | 10.63         | -            |

would be a problem, we chose pressures higher than the critical pressure of N<sub>2</sub> which is the component with the higher critical pressure. The experiments in this work are accompanied by classical MD calculations. Also, quantum mechanical calculations were performed to provide an ab initio PES, and scattering calculations were performed at energies corresponding to the average temperature of the experiments and at room temperature.

## 2. Methods

### 2.1. Experimental

Cylinders of argon and nitrogen were obtained from BOC gases and used without further purification. Measured volumes of these gases at constant pressures were used from these cylinders in order to produce mixtures of the two gases at the mole fractions shown in Table 1. In order to allow complete mixing, the mixtures were stored in separate cylinders for approximately one week. The flat plate pressure cell was made from an alloy of Ti and Zr in the mole ratio 0.676:0.324, which contributes almost zero coherent scattering to the diffraction pattern [50]. In the region of the neutron beam (30 mm × 30 mm), the pressure cell had front and back window thicknesses of 3.5 mm, and the gas occupied the space (3 mm) between the walls. The container was placed at right angle to the neutron beam. A gas handling rig was connected to the cell to control the pressure of the gas. A top loading closed cycle helium refrigerator was used to control the temperature within ± 1 K, using He exchange gas at 20 mbar to provide temperature uniformity. The employed temperature was  $T=1.02T_c$ , where  $T_c$  is the critical temperature of the mixture. The critical temperatures of the mixtures at the required mole fractions were predicted using Eq. (1) in ref. [48]. The properties ( $T_c$ ,  $P_c$ ,  $\rho_c$ ) of the mixtures shown in Table 1 were calculated using REFPROP [51] after our measurements.

Total neutron scattering measurements were performed on the NIMROD diffractometer at the ISIS pulsed neutron source [52]. Absolute values of the differential cross sections were obtained from the raw scattering data by normalising the data to the scattering from a

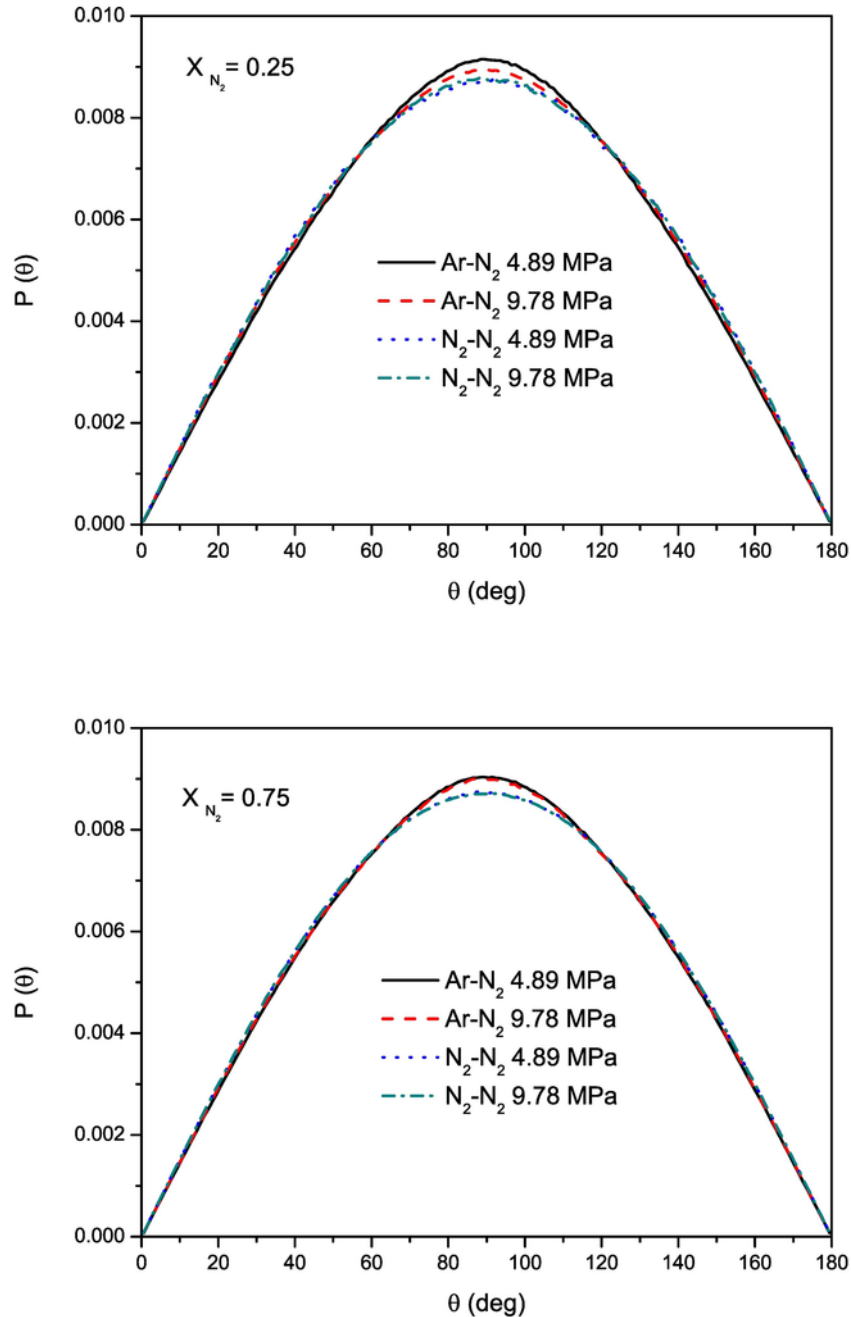


**Fig. 9.** Calculated angular distributions  $P(\theta)$  for intermolecular pairs of Ar-N<sub>2</sub> and N<sub>2</sub>-N<sub>2</sub> being located at distances smaller than the radius of the first coordination shell.

slab of vanadium of known thickness, and were further corrected for background and multiple scattering, container scattering and self attenuation, using the Gudrun data analysis program [53]. The data were put on absolute scale of barns per atom per sr by dividing by the number of atoms in the neutron beam ( $1 \text{ barn} = 10^{-28} \text{ m}^2$ ). The differential scattering cross sections presented here are further normalised to the square of the mean scattering length of each sample:

$$F(Q) = \frac{4x^2 b_N^2 H_{NN}(Q) + (1-x)^2 b_{Ar}^2 H_{ArAr}(Q) + 4x(1-x)b_N b_{Ar} H_{ArN}(Q)}{(2xb_N + (1-x)b_{Ar})^2}$$

where  $x$  is the mole fraction of N<sub>2</sub> in Ar, and the partial structure factor  $H_{\alpha\beta}(Q)$  is the three-dimensional Fourier transform of the corresponding site-site radial distribution function:

$$H_{\alpha\beta}(Q) = 4\pi\rho \int_0^\infty r^2 (g_{\alpha\beta}(r) - 1) \frac{\sin Qr}{Qr} dr \quad (2)$$

and  $\rho$  is the atomic number density. Note that the  $H_{NN}(Q)$  term includes both the intra- and inter-molecular scattering.

To interpret the total neutron scattering data, the experimental  $F(Q)$  were fit using the empirical potential structure refinement

**Table 3**  
MD results for self-diffusion coefficients of Ar-N<sub>2</sub> mixtures.

| $x_{N_2}$ | $T$ (K) | $P$ (bar) | $D_{N_2}$ ( $10^{-9}m^2/s$ ) | $D_{Ar}$ ( $10^{-9}m^2/s$ ) |
|-----------|---------|-----------|------------------------------|-----------------------------|
| 0.00      | 154.1   | 48.9      | -                            | 59.75                       |
|           |         | 97.8      | -                            | 13.51                       |
| 0.25      | 147.7   | 48.9      | 49.52                        | 45.36                       |
|           |         | 97.8      | 14.66                        | 13.72                       |
| 0.50      | 141.2   | 48.9      | 23.44                        | 23.00                       |
|           |         | 97.8      | 13.97                        | 14.13                       |
| 0.75      | 134.8   | 48.9      | 19.87                        | 18.74                       |
|           |         | 97.8      | 14.06                        | 14.07                       |
| 1.00      | 128.4   | 48.9      | 18.91                        | -                           |
|           |         | 97.8      | 13.89                        | -                           |

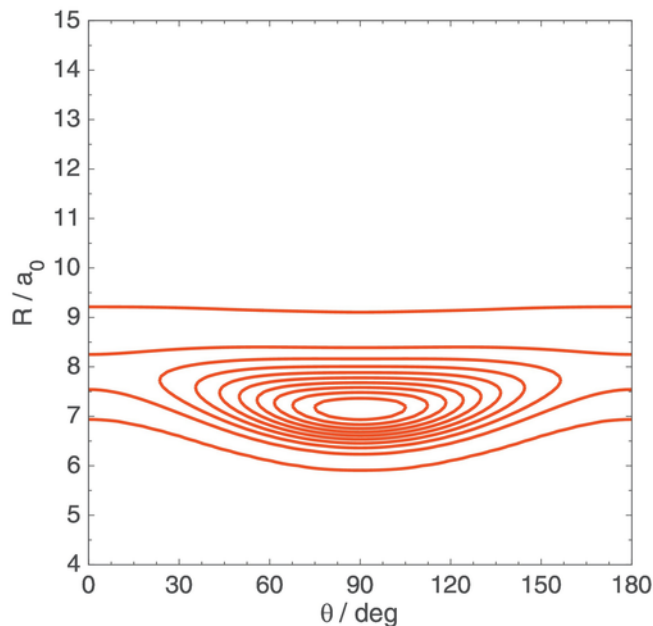


**Fig. 10.** Contour plot of the ground state wavefunction corresponding to bound state energy of  $-76.86\text{ cm}^{-1}$ .

(EPSR) procedure [54, 55]. The corresponding fits are shown alongside the data in Figs. 1 and 2. For each dataset a total number of 8000 particles, consisting of Ar atoms and N<sub>2</sub> molecules, were employed in simulation boxes of dimensions to give the specified number densities and mole ratios, Table 1. In this case a Lennard-Jones (LJ) potential was employed to describe each Ar and N atom, with additional charges of  $-0.482e$  on each of the N atoms and a counter charge of  $+0.964e$  on the centre-of-mass (com) of the dinitrogen molecule. There was no further refinement of the site-site empirical potentials, which were held at zero throughout all the EPSR simulations shown here. All potentials were truncated at a distance of  $18\text{ \AA}$ .

Initially, LJ parameters identical to those described in the MD Section 2.2.1 and a nitrogen bond length of  $1.12\text{ \AA}$  were employed. Although these initial EPSR simulations could reproduce the high- $Q$  data, the agreement at low- $Q$  was not satisfactory. There was a mismatch in the position of the main diffraction peak near  $Q=2\text{ \AA}^{-1}$ , and the rise at low  $Q$  was too large in the simulation apart from the case of pure Ar, where the quality of the neutron data is poor because of the weak signal. For that reason, a modified LJ potential was developed to give a closer fit to the neutron data. The values of the LJ parameters so obtained were  $\epsilon/k_B = 114.25\text{ K}$  and  $\sigma = 3.345\text{ \AA}$  for Ar, and  $\epsilon/k_B = 30.30\text{ K}$  and  $\sigma = 3.430\text{ \AA}$  for N. The average bond length found in the EPSR simulations was  $1.09\text{ \AA}$ , with a RMS deviation of

$0.048\text{ \AA}$  corresponding to the zero-point quantum effect. It can be seen that both data and EPSR simulations, Figs. 1 and 2, follow the qualitative behaviour of the  $Q=0$  limit of  $F(Q)$ , Table 1, although some discrepancies exist due to the difficulty of getting accurate data at the lowest  $Q$  values, particularly for the lowest density pure Ar data where the diffraction signal is weakest.

## 2.2. Computational

### 2.2.1. Classical molecular dynamics

Classical molecular dynamics simulations in the NPT and the NVT ensemble were performed for pure supercritical Ar and N<sub>2</sub>, as well as their binary mixtures. The mole fraction of N<sub>2</sub> in the simulated mixtures was 0.25, 0.50 and 0.75, respectively. The thermodynamic state points of the simulated systems corresponded to a temperature of  $T=1.02 T_c$ , where  $T_c$  is the experimental critical temperature of each system (pure and mixture), and to pressures of 48.9 and 97.8 bar.

In all simulations, a cubic box containing in total 500 molecules (atoms in the case of Ar) was used and periodic boundary conditions were also employed. The selection of the force fields for Ar and N<sub>2</sub> had to ensure that the employed potential models predict with very good accuracy the critical temperature of the fluids, since the experimental measurements were performed very close to the critical temperature. Several trial tests were performed in order to ensure that the computationally predicted phase behaviour of the fluids at the experimental conditions does not correspond to vapour-liquid equilibrium but to the supercritical phase. Our tests suggested that the LJ potential model developed by Vrabcic et al. [56] for Ar ( $\epsilon/k_B = 116.79\text{ K}$ ,  $\sigma = 3.3952\text{ \AA}$ ), and the non-polarizable all-atom transferable potential for phase equilibria, TraPPE, force field [40] for N<sub>2</sub> were sufficient to describe the mixtures. The reason for this is that these force fields have been developed in order to predict very accurately the critical point of the systems and therefore they have been selected to be used in our simulation studies. The potential for N<sub>2</sub> employs a 12-6 LJ potential for each N atom ( $\epsilon/k_B = 36.0\text{ K}$ ,  $\sigma = 3.31\text{ \AA}$ ) which are separated by  $1.10\text{ \AA}$ . It also includes point charges at the nitrogen atoms ( $q = -0.482e$ ), and a charge ( $-2q = +0.964e$ ) on the centre-of-mass (com) of N<sub>2</sub> to account for the quadrupole moment of molecular nitrogen and achieve charge neutrality.

NPT-MD simulations were first performed to predict the densities of the systems under investigation and then NVT-MD simulations were carried out at the calculated densities in order to calculate the structural, transport and dynamic properties of the fluids. The simulated systems were equilibrated for 2 ns in all simulations and the system properties were obtained in subsequent 1 ns production runs. The equations of motion were integrated using a leapfrog-type Verlet algorithm and the integration time step was set to 1 fs. A Nose-Hoover thermostat and barostat with a temperature relaxation time of 0.5 and 1.0 ps, respectively, were used to constrain the temperature and the pressure during the simulations. The intramolecular geometry of N<sub>2</sub> molecules was constrained using the quaternion formalism. A cut-off radius of  $12.0\text{ \AA}$  was applied for the intermolecular interactions and long-range corrections were also taken into account. The Ewald summation technique was employed to account for the long-range electrostatic interactions.

### 2.2.2. Ab initio potential energy surfaces and quantum scattering calculations

We carried out closed-shell explicitly correlated coupled-cluster calculations with single-, double-, and non-iterative triple-excitations [CCSD(T)-F12a] [57, 58] for the Ar-N<sub>2</sub>( $X^1\Sigma_g^+$ ) complex. The cou-

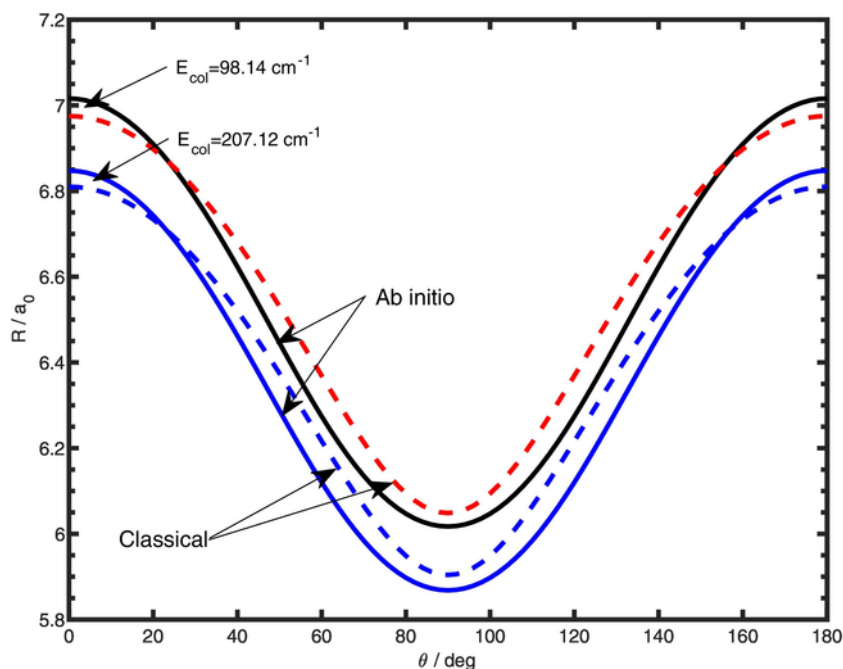


**Fig. 11.** Comparison of the quantum mechanical (solid line) and classical (dashed line) Ar-N<sub>2</sub> interaction potential from this work at a collision energy of 98.139 and 207.12 cm<sup>-1</sup>.

**Table 4**

Bound states (in cm<sup>-1</sup>) of Ar-N<sub>2</sub> complex supported by the CCSD(T)-F12a PES for values of  $J=0$  to 4 for the total parity  $p=+1$ .

| n  | $J=0$   | $J=1$   | $J=2$   | $J=3$   | $J=4$   |
|----|---------|---------|---------|---------|---------|
| 1  | -76.859 | -76.723 | -76.450 | -76.041 | -75.496 |
| 2  | -59.629 | -60.457 | -67.164 | -66.763 | -66.228 |
| 3  | -46.731 | -59.460 | -60.279 | -59.996 | -59.599 |
| 4  | -40.199 | -46.611 | -59.131 | -58.654 | -58.036 |
| 5  | -28.447 | -40.475 | -46.371 | -46.011 | -45.532 |
| 6  | -25.072 | -39.967 | -43.034 | -42.698 | -42.250 |
| 7  | -18.248 | -28.338 | -40.356 | -40.116 | -40.181 |
| 8  | -11.934 | -25.011 | -39.585 | -39.073 | -39.750 |
| 9  | -9.347  | -23.743 | -28.184 | -35.430 | -38.436 |
| 10 | -6.298  | -19.467 | -28.108 | -27.866 | -34.886 |
| 11 | -2.392  | -18.115 | -24.877 | -27.740 | -27.454 |
| 12 | -0.538  | -11.841 | -23.429 | -24.654 | -27.239 |
| 13 | 0.000   | -9.255  | -22.282 | -22.979 | -24.332 |
| 14 | 0.000   | -7.887  | -19.255 | -21.951 | -22.408 |
| 15 | 0.000   | -6.202  | -17.849 | -18.934 | -21.509 |
| 16 | 0.000   | -2.332  | -11.655 | -17.453 | -18.502 |
| 17 | 0.000   | -0.498  | -9.070  | -11.377 | -16.930 |
| 18 | 0.000   | 0.000   | -8.309  | -11.315 | -14.021 |
| 19 | 0.000   | 0.000   | -7.586  | -8.798  | -11.007 |
| 29 | 0.000   | 0.000   | -6.010  | -8.086  | -10.813 |
| 21 | 0.000   | 0.000   | -4.181  | -7.181  | -8.440  |
| 22 | 0.000   | 0.000   | -2.212  | -5.719  | -7.745  |
| 23 | 0.000   | 0.000   | -0.418  | -3.857  | -6.685  |
| 24 | 0.000   | 0.000   | 0.000   | -2.032  | -5.327  |
| 25 | 0.000   | 0.000   | 0.000   | -0.302  | -3.425  |
| 26 | 0.000   | 0.000   | 0.000   | 0.000   | -1.794  |
| 27 | 0.000   | 0.000   | 0.000   | 0.000   | -0.154  |

pled-cluster method is currently a state-of-the-art method that can recover most of the correlation energy, which is very important in the dispersion-bound van der Waals complexes such as Ar-N<sub>2</sub>. We performed CCSD(T)-F12a calculations with the augmented correlation consistent triple-zeta basis (aug-cc-pVTZ) [59-62] supplemented with mid-bond functions (3s3p2d2f1g1h). The bond functions were described by placing dummy atom in the half distance between Ar and

**Table 5**

Bound states (in cm<sup>-1</sup>) of Ar-N<sub>2</sub> complex supported by the CCSD(T)-F12a PES for values of  $J=1$  to 4 for the total parity  $p=-1$ .

| n  | $J=1$   | $J=2$   | $J=3$   | $J=4$   |
|----|---------|---------|---------|---------|
| 1  | -60.408 | -67.164 | -66.763 | -66.228 |
| 2  | -40.358 | -60.141 | -59.740 | -59.206 |
| 3  | -23.783 | -43.033 | -42.696 | -42.247 |
| 4  | -19.443 | -40.088 | -39.683 | -40.181 |
| 5  | -7.882  | -28.172 | -35.430 | -39.145 |
| 6  | 0.000   | -23.535 | -27.812 | -34.886 |
| 7  | 0.000   | -22.282 | -23.164 | -27.333 |
| 8  | 0.000   | -19.186 | -21.949 | -22.673 |
| 9  | 0.000   | -8.313  | -18.800 | -21.502 |
| 10 | 0.000   | -7.569  | -11.315 | -18.288 |
| 11 | 0.000   | -4.181  | -8.103  | -14.021 |
| 12 | 0.000   | 0.000   | -7.138  | -10.814 |
| 13 | 0.000   | 0.000   | -3.857  | -7.789  |
| 14 | 0.000   | 0.000   | 0.000   | -6.599  |
| 15 | 0.000   | 0.000   | 0.000   | -3.424  |

**Table 6**

Comparison for selected Ar-N<sub>2</sub> transitions between this work, previous results of Munteanu et al. [14] and experimental results of Jäger et al. [13] (in cm<sup>-1</sup>).

| $J'_{K'_a K'_c} - J''_{K''_a K''_c}$ | Expt., ref. [13] | Calc., this work | Calc., ref [14] |
|--------------------------------------|------------------|------------------|-----------------|
| 1 <sub>01</sub> -0 <sub>00</sub>     | 0.136945         | 0.136417         | 0.135934        |
| 2 <sub>02</sub> -1 <sub>01</sub>     | 0.273842         | 0.272786         | 0.271825        |
| 3 <sub>03</sub> -2 <sub>02</sub>     | 0.410644         | 0.409061         | 0.409250        |
| 4 <sub>04</sub> -3 <sub>03</sub>     | 0.547304         | 0.545192         | 0.545447        |
| 5 <sub>05</sub> -4 <sub>04</sub>     |                  | 0.681131         | 0.681455        |
| 2 <sub>12</sub> -1 <sub>11</sub>     | 0.268252         | 0.267338         | 0.266321        |
| 3 <sub>13</sub> -2 <sub>12</sub>     | 0.402248         | 0.400914         | 0.399353        |
| 4 <sub>14</sub> -3 <sub>13</sub>     | 0.536087         | 0.534378         | 0.532225        |
| 5 <sub>15</sub> -4 <sub>14</sub>     |                  | 0.667693         | 0.667275        |

centre of mass of the N<sub>2</sub> molecule and constructed with the following exponents: (3s3p : 0.9,0.3,0.1), (2d2f : 0.6,0.2), (gh : 0.3). We used the scaled F12 triples correction [58] as implemented in

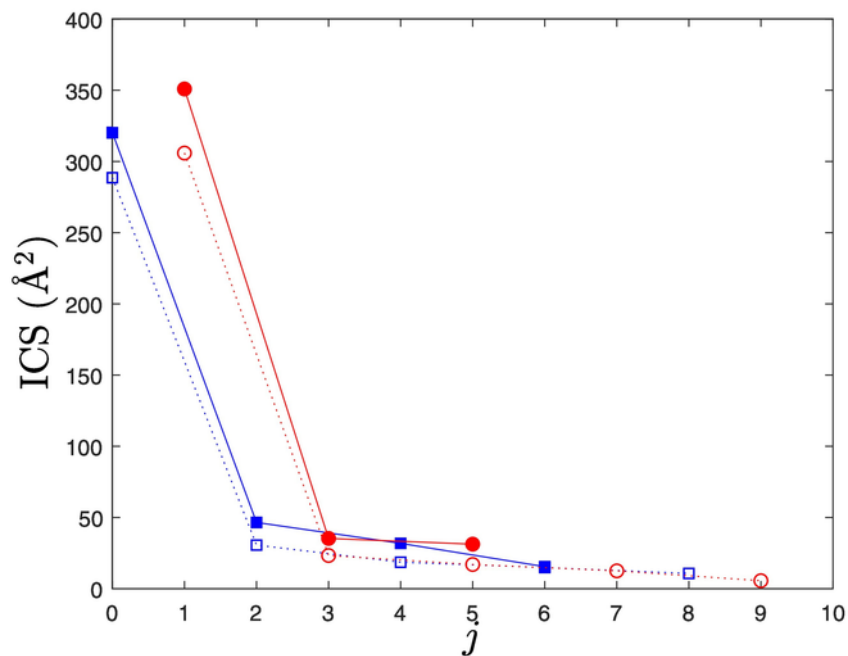


**Fig. 12.** Comparison of calculated ICS for  $\text{Ar} + \text{ortho-N}_2 (v=0, j=0) \rightarrow \text{Ar} + \text{ortho-N}_2 (v=0, j=0-8)$  at  $E_{\text{col}}$  of  $98.139$  and  $207.12 \text{ cm}^{-1}$  (filled and empty blue squares, respectively) and  $\text{Ar} + \text{para-N}_2 (v=0, j=1) \rightarrow \text{Ar} + \text{para-N}_2 (v=0, j=1-9)$  at  $E_{\text{col}}$  of  $98.139$  and  $207.12 \text{ cm}^{-1}$  (filled and empty red circles, respectively) as a function of the final  $\text{N}_2$  level.

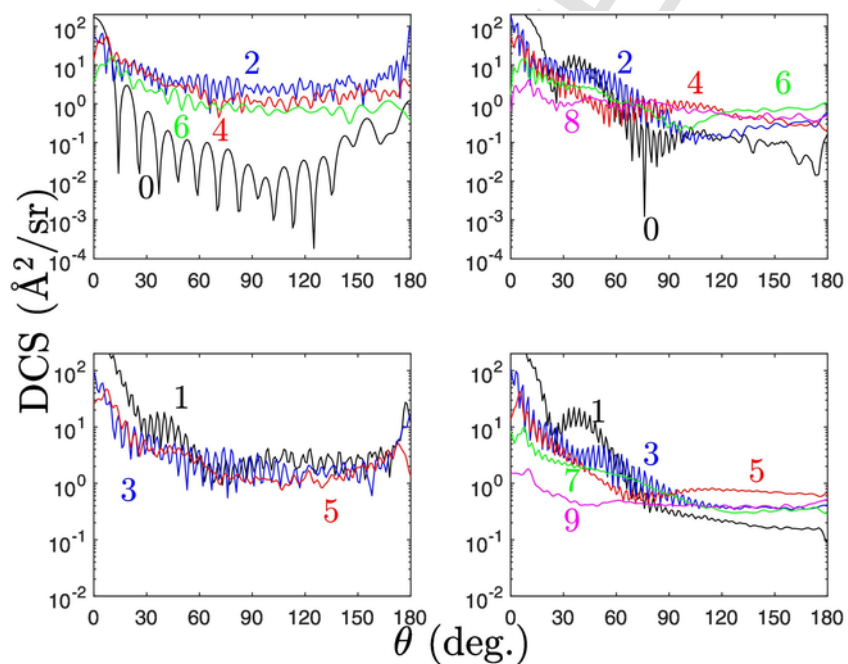


**Fig. 13.** Upper panel: comparison of calculated DCS for  $\text{Ar} + \text{ortho-N}_2 (v=0, j=0) \rightarrow \text{Ar} + \text{ortho-N}_2 (v=0, j=0-8)$  collisions at  $E_{\text{col}}$  of  $98.139$  and  $207.12 \text{ cm}^{-1}$  (left and right, respectively). The final  $\text{N}_2$  levels are shown on the figure. Lower panel: as previously, but for  $\text{Ar} + \text{para-N}_2 (v=0, j=1) \rightarrow \text{Ar} + \text{para-N}_2 (v=0, j=1-9)$  collisions.

MOLPRO [63] to estimate the effect of explicit correlated treatment on the triple corrections which are not explicitly-correlated as currently implemented. To determine interaction energies necessary to construct the potential energy surface (PES) from the CCSD(T)-F12 calculations we applied the counterpoise method of Boys and Bernardi [64] to estimate the basis set superposition error (BSSE), in

which we subtract the energies of the fragments computed in the dimer centred atomic orbital basis. The interaction energy is defined as

$$V(R, \theta) = E^{(\text{Ar-N}_2)}(R, \theta) - E^{(\text{Ar})}(R, \theta) - E^{(\text{N}_2)}(R, \theta). \quad (3)$$

Electronic structure calculations were performed on a two-dimensional grid of Jacobi coordinates composed of 42 radial distances from  $R=3.5a_0$  to  $30a_0$  with a step of  $0.25a_0$  (between 3.5 and 10  $a_0$ ),  $0.5a_0$  (between 10 and 12  $a_0$ ),  $1.0a_0$  (between 12 and 16  $a_0$ ) and  $2.0a_0$  (between 16 and 30  $a_0$ ). The Jacobi  $R$  distance of Ar is measured from the centre of mass of the  $N_2$  molecule and the  $N_2$  diatomic distance was fixed at the equilibrium value of  $r=2.0743a_0$ . The Jacobi angle  $\theta$  describing the rotation of the Ar around  $N_2$  molecule was represented by 10 grid values with a step of  $10^\circ$  from  $0^\circ$  to  $90^\circ$ . The total grid therefore is composed of 420 *ab initio* points.

In order to perform scattering calculations we needed to fit the discrete set of PES points to analytical expression. We expand the angular dependence of the PES in the series of Legendre polynomials  $P_l^0(\cos \theta)$  restricted to even-valued  $l$  index due to homonuclearity of the  $N_2$  molecule:

$$V(R, \theta) = \sum_{l=0}^9 V_{12}(R) P_{2l}^0(\cos \theta). \quad (4)$$

The long-range,  $V_{lr}$ , of the PES for the distances  $R > 20a_0$  is fitted to the following expansion involving  $C_n$  dispersion coefficients:

$$V_{lr}(R, \theta) = \sum_{n=3}^5 \sum_{l=0}^{2n-4} \frac{C_{2n,2l}}{R^{2n}} P_{2l}^0(\cos \theta). \quad (5)$$

The radial coefficients from the angular expansion of the PES are represented by Reproducing Kernel Hilbert Space (RKHS) interpolation method [65] with a radial kernel of  $R^{-6}$  type. The final fitted PES is then composed of the Legendre expansion and long-range expansion by smoothly gluing them together in the long-range by hyperbolic tangent function. The first few radial expansion coefficients  $V_{12}(R)$  are shown in Fig. 3. One can see that  $V_8$  radial coefficients is already quite small in the region of the global minimum.

The contour plot of the fitted Ar- $N_2$  PES is shown in Fig. 4. The global minimum with  $D_e=98.66 \text{ cm}^{-1}$  is located at the T-shaped geometry (i.e.,  $\theta_e=90^\circ$ ) at the equilibrium distance of  $R_e=7.00a_0$ . The collinear geometries for  $\theta=0^\circ$  or  $\theta=180^\circ$  represent saddle points at  $R=8.04a_0$  and energy of  $-75.33 \text{ cm}^{-1}$ .

We performed bound state calculations for the Ar- $^{14}N_2$  van der Waals complex using the new PES developed in this work. The dissociation energy of the complex was determined to be  $D_0=76.86 \text{ cm}^{-1}$ . The bound states were calculated using the radial numerical basis set functions obtained from one-dimensional distributed Gaussian basis set calculations on the radial cut passing through global minimum. We used 30 radial basis functions, and angular basis constructed with rotational functions of  $N_2$  up to  $j_{\max}=16$  with a  $N_2$  rotational constant of  $1.98957 \text{ cm}^{-1}$ .

The  $^{14}N_2$  exists in separate *ortho* levels (with total nuclear spin  $I=0$  or 2) and *para* levels (with  $I=1$ ) because of the non-zero nuclear spin of  $^{14}N$  ( $I=1$ ). The *ortho* to *para* ratio is 2:1, with the *ortho* populating only even ( $j=0,2,\dots$ ) levels, and the *para* only odd ( $j=1,3,\dots$ ) levels. Integral (ICS) and differential (DCS) cross sections were obtained using the HIBRIDON program [66]. The wavefunction was propagated using the improved log-derivative propagator by Manolopoulos and co-workers [67, 68]. We followed closely the approach presented in previous work on Ar/Xe +  $N_2$  collisions [69, 70]. A rigid rotor model with rotational constant,  $B$ , of  $1.98957 \text{ cm}^{-1}$  was used to describe the  $N_2$  molecule and the reduced mass of the Ar- $N_2$  system was  $16.46621 \text{ amu}$ . Calculations were performed for total en-

ergies up to  $1435$  and  $1534 \text{ cm}^{-1}$  for systems containing *ortho* and *para* systems, respectively. The maximum value of the rotational quantum number of the  $N_2$  molecule was 60, and the maximum value of the total angular momentum quantum number was 310.

### 3. Results and discussion

#### 3.1. Intermolecular structure and transport coefficients

The intermolecular structure of the mixtures has been studied in terms of the experimental pair radial distribution functions ( $g(r)$  or RDFs) which are shown in Figs. 5 and 6 for the pressures of around 49 bar and 92–98 bar, respectively. The  $g(r)$  shown in Figs. 5 and 6 have been obtained using the experimental structure factors, the empirical potential structure refinement (EPSR) simulations and the modified LJ described in Section 2.1.

The RDFs shown in Figs. 5 and 6 are for Ar–Ar, Ar–N, Ar– $N_2(\text{com})$ , N–N, N– $N_2(\text{com})$ , and  $N_2(\text{com})$ – $N_2(\text{com})$  separations, where for simplicity in notation we use  $N_2(\text{com})$  to denote the centre of mass of the dinitrogen molecule. The MD  $g(r)$  distributions at 48.9 bar and 97.8 bar are shown in Fig. 7. We note that all these  $g(r)$  show similar shape and exhibit two peaks, with the second peak of a significantly lower intensity compared with the first peak. The existence of a clear first minimum in the RDF suggests the formation of a first coordination shell around each molecule. At higher pressures a clear second minimum is observed because at these conditions the mixtures exhibit a liquid-like microscopic structure [70, 71]. At all the pressures studied in this work, the height of the first peak decreases in the following order: Ar–Ar > Ar– $N_2(\text{com})$  > Ar–N and  $N_2(\text{com})$ – $N_2(\text{com})$  > N– $N_2(\text{com})$  > N–N. Regarding the positions of the first peak: Ar–Ar < Ar–N  $\approx$  Ar– $N_2(\text{com})$ . We also note that the concentration effect on the shape of the RDF is not strong at high pressures.

A comparison between some representative EPSR and MD atom-atom RDFs is shown in Fig. 8. Although the comparison is shown for the pressure of 48.9 bar, the agreement is very good for the higher pressure as well. The EPSR and MD produce similar RDFs but the former is somewhat better in reproducing the total structure factors. As shown in Table 2, the densities from the MD are in good agreement with the predictions using REFPROP [51], which were used in the EPSR simulations.

In order to investigate the local composition in the simulated mixtures, the first shell coordination numbers corresponding to the com-com RDFs were also obtained. The coordination numbers that were calculated using a cut-off distance of  $5.95 \text{ \AA}$  which corresponds to the first coordination shell, are presented in Table 2. Using these coordination numbers, the local mole fractions in the first solvation shell of each individual Ar and  $N_2$  have been calculated. These local mole fractions reach their bulk values at very short distances in the range of the first solvation shell. This shows that local composition enhancement and aggregation effects are not pronounced in these mixtures. Similar analysis was employed in previous studies. For example, strong aggregation effects between the ethanol cosolvent molecules in  $\text{CO}_2$ - $\text{CH}_3\text{CH}_2\text{OH}$  was observed [72, 73]. As in the case of supercritical  $\text{CO}_2$ - $\text{CH}_4$  mixtures [74], no aggregation effects were observed in the Ar- $N_2$  systems studied here.

Apart from the calculated atom-atom RDFs, the local orientational order in the mixtures was investigated by calculating angular distributions for pairs of Ar- $N_2$  and  $N_2$ - $N_2$  molecules. The pairs taken into account in the calculations have an intermolecular (com-com) distance less than or equal to  $5.95 \text{ \AA}$  which corresponds to the first coordination shell radius. In the case of the  $N_2$ - $N_2$  pairs,  $\theta$  is defined as

the angle between the N-N bond vectors of the two  $N_2$  molecules. In the case of Ar- $N_2$  pairs,  $\theta$  is the angle between the Ar- $N_2(\text{com})$  vector and the N-N bond vector of the  $N_2$  molecule. The calculated normalized angle distributions  $P(\theta)$  for some representative mixtures are shown in Fig. 9. These distributions exhibit peaks at about  $90^\circ$  and their average  $\theta$  values are also very close to  $90^\circ$ , due to the symmetry of the obtained distributions. It is interesting to notice that this behaviour is obtained for both Ar- $N_2$  and  $N_2$ - $N_2$  pairs, signifying that the so-called T-shaped dimer structures are preferred in these supercritical mixtures. The shape of the obtained distribution does not change in the range of pressures and compositions studied, indicating that pressure-induced orientational order effects [75] are not important at these conditions.

The self-diffusion coefficients of both components in the mixture were obtained from the MD calculations using the Einstein equation and the linear region of the mean squared displacement (MSD) versus time. Results for all the mole fractions are shown in Table 3. To the best of our knowledge, there are not any experimental measurements of the self-diffusion coefficients at the thermodynamic state points employed in the neutron scattering measurements.

### 3.2. Quantum calculations of bound states and scattering

The contour plot of the rovibrational ground state wavefunction for the Ar- $N_2$  van der Waals complex is shown in Fig. 10. This wavefunction has a maximum for the T-shaped geometry but has a significant amplitude also for the collinear geometries meaning that the rotation of the  $N_2$  molecule is not much hindered. The average expectation value of  $R$  calculated with this wavefunction is  $\langle R \rangle = 7.304a_0$  and the rotational constant of the complex  $B_0 = 0.069 \text{ cm}^{-1}$ . This calculated rotational constant agrees well with the experimental one of  $0.071 \text{ cm}^{-1}$  from Jäger et al. [13]. A comparison between the ab initio and the classical potential used in the MD simulations is shown in Fig. 11 for two collision energies which correspond to the average temperature of the experiments ( $141 \text{ K} = 98.14 \text{ cm}^{-1}$ ) and to the room temperature ( $298 \text{ K} = 207.12 \text{ cm}^{-1}$ ). The differences between the two potentials are small; the MD potential is more attractive than the ab initio at  $\theta = 90^\circ$  but the reverse is true at  $\theta = 0^\circ$  (and by symmetry at  $\theta = 180^\circ$ ). These findings are in excellent agreement with the results obtained by the angular distributions presented in Fig. 9, indicating that the T-shaped Ar- $N_2$  and  $N_2$ - $N_2$  dimer structures are predominant in the supercritical mixtures under study.

The full set of bound states for the Ar- $N_2$  complex for the total angular momentum quantum numbers from  $J=0$  to  $J=4$  is shown in Tables 4 and 5 for the total parity  $+1$  and  $-1$ , respectively. Our calculated bound states can be compared to previous theoretical results of Munteanu et al. [14] and experimental results of Jäger et al. [13]. We show this comparison in Table 6 for selected  $J_{K_a'K_c'}^J - J_{K_a''K_c''}^J$  transitions, where  $J$  is a total angular quantum number and  $K_a$  and  $K_c$  its projection quantum numbers of the asymmetric rotor. The agreement between the experimental and previous results is excellent showing that our new PES is of good quality and can be used to determine other properties of the Ar- $N_2$  complex.

A comparison between calculated QM ICS for Ar + *ortho*- $N_2$  ( $v, j = 0, 2$ ) and Ar + *para*- $N_2$  ( $v, j = 1, 3$ ) for various final  $N_2$  rotational levels at a collision energy of  $98.139$  and  $207.12 \text{ cm}^{-1}$  is shown in Fig. 12. The cross sections exhibit high values for the elastic collisions. The ICS decreases with increasing energy gap between the initial and final levels in inelastic collisions. Regarding inelastic excitation from the lowest  $N_2$  rotational levels, the Ar + *ortho*- $N_2$  ICS are higher than the Ar + *para*- $N_2$ . The same trend was observed in the similar Xe +  $N_2$  system at  $241 \text{ cm}^{-1}$  by Dellis et al. [70]. Comparing

the values of Xe +  $N_2$  ICS presented there with the Ar +  $N_2$  ICS obtained in our study we observe that for inelastic excitation from the lowest  $N_2$  rotational transitions, Ar + *para*- $N_2$  ICS are higher than Xe + *para*- $N_2$ . The same trend is observed in collisions with *ortho*- $N_2$  for high final  $N_2$  rotational levels and the reverse is true for low final levels. The differences in the ICS between Ar- $N_2$  and Xe- $N_2$  arise both because of the different reduced masses ( $16.47$  and  $23.09 \text{ amu}$ , respectively) but also because the intermolecular potential is more attractive in the Xe +  $N_2$  case (the well depths are  $99$  and  $120 \text{ cm}^{-1}$ , respectively). Future work will examine the role of the mass in this difference and provide the thermal rate coefficients from the calculated cross sections.

The DCS for Ar + *ortho*- $N_2$  ( $v, j = 0$ ) and Ar + *para*- $N_2$  ( $v, j = 1$ ) collisions at a collision energy of  $98.139$  and  $207.12 \text{ cm}^{-1}$  are shown in Fig. 13 for various final  $N_2$  rotational levels. The DCS exhibit oscillations due to quantum interference like in the Ar + NO collisions [76]. As discussed by Dellis et al. [70], these oscillations are much more pronounced in collisions of a rare gas and molecular nitrogen because of the more homonuclear terms in the interaction potential compared with the Ar + NO, where heteronuclear terms also exist. The DCS exhibit more backwards scattering for collisions of Ar + *ortho*- $N_2$  than in the Ar + *para*- $N_2$  case. The same effect was observed in Xe +  $N_2$  collisions [70]. The DCS exhibit a preference for forward scattering especially for low rotational excitations at  $207.12 \text{ cm}^{-1}$ . At  $98.139 \text{ cm}^{-1}$ , the DCS exhibit a more symmetric shape possibly because of the production and breaking of an intermediate van der Waals complex. Future work will provide information on the energy dependence of the stereodynamics in Rg +  $N_2$  collisions.

## 4. Conclusions

Neutron scattering experiments were reported for the first time on supercritical Ar- $N_2$  mixtures for temperatures between  $128.4$  and  $154.1 \text{ K}$  and pressures between  $48.7$  and  $97.8 \text{ bar}$ . The experiments provided information regarding the microscopic structure which was shown to be not very sensitive to the mole fractions. Future experiments using  $^{36}\text{Ar}$  and/or X-rays may improve significantly the signal-to-noise ratio.

The MD calculations, which employed well-established potential models, agreed well with the experiments and provided also the values of the diffusion coefficients. As shown by calculating the local coordination numbers and the corresponding local mole fractions, local composition enhancement and aggregation effects are not pronounced in these Ar- $N_2$  mixtures near their critical temperatures.

A new ab initio PES was developed and the intermolecular potential was in reasonable agreement with the MD model. The PES was employed for bound calculations and to provide ICS and DCS for rotational excitation at collision energies relevant to the experimental temperature and also to the room temperature. Future work will provide the thermally averaged rate coefficients for Ar +  $N_2$  inelastic collisions, and compare the classical MD with quantum Born-Oppenheimer MD simulations.

## Declaration of Competing Interest

There are no conflicts to declare.

## Acknowledgments

S.M. acknowledges useful discussions with the late Professor J. S. Rowlinson (Oxford) and Dr E. W. Lemmon (NIST) on previous pVT

work. Neutron beam time at ISIS and project funding was provided by the Science and Technology Facilities Council (RB1620044). We acknowledge Chris Goodway and Thomas Headen (Rutherford Appleton Laboratory) for their help with the neutron scattering experiments. This research utilized Queen Mary's MidPlus computational facilities, supported by QMUL Research-IT, <http://doi.org/10.5281/zenodo.438045>. The MD calculations were performed using the computational facilities of the Laboratory of Physical Chemistry, University of Athens. J.K. acknowledges financial support from the U.S. National Science Foundation, under the grant no. CHE-1565872 to M. H. Alexander.

## References

- [1] O. Kajimoto, Solvation in supercritical fluids: its effects on energy transfer and chemical reactions, *Chem. Rev.* 99 (1999) 355–389.
- [2] S.C. Tucker, Solvent density inhomogeneities in supercritical fluids, *Chem. Rev.* 99 (1999) 391–418.
- [3] I. Skarmoutsos, E. Guardia, Local structural effects and related dynamics in supercritical ethanol. 1. Mechanisms of local density reorganization and residence dynamics, *J. Phys. Chem. B* 113 (2009) 8887–8897.
- [4] G.G. Simeoni, T. Bryk, F.A. Gorelli, M. Krisch, G. Ruocco, M. Santoro, T. Scopigno, The Widom line as the crossover between liquid-like and gas-like behaviour in supercritical fluids, *Nat. Phys.* 6 (2010) 503–507.
- [5] D. Bolmatov, V.V. Brazhkin, K. Trachenko, Thermodynamic behaviour of supercritical matter, *Nat. Commun.* 4 (2013) 2331.
- [6] I. Skarmoutsos, E. Guardia, J. Samios, Local structural fluctuations, hydrogen bonding and structural transitions in supercritical water, *J. Supercrit. Fluids* 130 (2017) 156–164.
- [7] I.B. Petsche, P.G. Debenedetti, Solute-solvent interactions in infinitely dilute supercritical mixtures: a molecular dynamics investigation, *J. Chem. Phys.* 91 (1989) 7075–7084.
- [8] E.W. Lemmon, R.T. Jacobsen, Thermodynamic properties of mixtures of nitrogen, argon, and oxygen, including air, *Adv. Cryog. Eng.* 43 (1998) 1281–1288.
- [9] E.W. Lemmon, R.T. Jacobsen, S.G. Penoncello, D.G. Friend, Thermodynamic properties of air and mixtures of nitrogen, argon, and oxygen from 60 to 2000 K at pressures to 2000 MPa, *J. Phys. Chem. Ref. Data* 29 (2000) 331–385.
- [10] O. Kunz, R. Klimeck, W. Wagner, M. Jaeschke, The GERG-2004 wide-range equation of state for natural gases and other mixtures, GERG TM15, 2007; *Fortschr.-Ber. VDI, Reihe 6, Nr. 557*, VDI Verlag, Düsseldorf, 2007, Also available as GERG Technical Monograph 15.
- [11] O. Kunz, W. Wagner, The GERG-2008 wide-range equation of state for natural gases and other mixtures: an expansion of GERG-2004, *J. Chem. Eng. Data* 57 (2012) 3032–3091.
- [12] J. Gernert, R. Span, EOS-CG: a Helmholtz energy mixture model for humid gases and CCS mixtures, *J. Chem. Thermodyn.* 93 (2016) 274–293.
- [13] W. Jäger, M.C.L. Gerry, C. Bissonnette, F.R.W. McCourt, Pure rotational spectrum of, and potential-energy surface for, the Ar-N<sub>2</sub> Van der Waals complex, *Faraday Discuss.* 97 (1994) 105–118.
- [14] C.R. Munteanu, J.L. Cacheiro, B. Fernández, Accurate intermolecular ground state potential of the Ar-N<sub>2</sub> van der Waals complex, *J. Chem. Phys.* 121 (2004) 10419–10425.
- [15] A.K. Dham, W.J. Meath, J.W. Jechow, R.W. McCourt, New exchange-Coulomb N<sub>2</sub>-Ar potential-energy surface and its comparison with other recent N<sub>2</sub>-Ar potential-energy surfaces, *J. Chem. Phys.* 124 (2006) 034308.
- [16] C. Wu, C. Wu, D. Song, H. Su, X. Xie, M. Li, Y. Deng, Y. Liu, Q. Gong, Communication: determining the structure of the N<sub>2</sub>/Ar van der Waals complex with laser-based channel-selected Coulomb explosion, *J. Chem. Phys.* 140 (2014) 141101.
- [17] H. Fu, R. Zheng, L. Zheng, Theoretical studies of three-dimensional potential energy surfaces using neural networks and rotational spectra of the Ar-N<sub>2</sub> complex, *Mol. Phys.* 114 (2016) 72–82.
- [18] O.G. Danylchenko, S.I. Kovalenko, V.N. Samovarov, Structure of mixed clusters formed in supersonic jets of Ar-N<sub>2</sub> gas mixtures, *Low Temp. Phys.* 33 (2007) 1403–1407.
- [19] C.S. Barrett, L. Meyer, Argon-nitrogen phase diagram, *J. Chem. Phys.* 42 (1965) 107–112.
- [20] W. Press, B. Janik, H. Grimm, Frozen-in orientational disorder in mixtures of solid nitrogen and argon, *Z. Phys. B* 49 (1982) 9–16.
- [21] W. Langel, Inelastic neutron scattering from matrix isolated species, *Spectrochim. Acta A* 48 (1992) 405–427.
- [22] J.L. Yarnell, M.J. Katz, R.G. Wenzel, S.H. Koenig, Structure factor and radial distribution function for liquid argon at 85 °K, *Phys. Rev. A* 7 (1973) 2130–2144.
- [23] I.M. de Schepper, P. Verkerk, A. van Well, L.A. de Graaf, Short-wavelength sound modes in liquid argon, *Phys. Rev. Lett.* 50 (1983) 974–977.
- [24] I.M. de Schepper, P. Verkerk, A.A. van Well, L.A. de Graaf, Non-analytical dispersion relations in liquid argon, *Phys. Lett.* 104A (1984) 29–32.
- [25] A.A. van Well, P. Verkerk, L.A. de Graaf, J.-B. Suck, J.R.D. Copley, Density fluctuations in liquid argon: coherent dynamic structure factor along the 120-K isotherm obtained by neutron scattering, *Phys. Rev. A* 31 (1985) 3391–3414.
- [26] H. Fredrikze, J.B. van Tricht, A.A. van Well, R. Magli, P. Chieux, F. Barocchi, Pair potential from neutron diffraction on argon at low densities, *Phys. Rev. Lett.* 62 (1989) 2612–2615.
- [27] U. Bafle, P. Verkerk, F. Barocchi, L.A. de Graaf, J. Suck, H. Mutka, Onset of departure from linearized hydrodynamic behavior in argon gas studied with neutron Brillouin scattering, *Phys. Rev. Lett.* 65 (1990) 2394–2397.
- [28] B. Mos, P. Verkerk, U. Bafle, C. Benmore, J.B. Suck, F. Barocchi, J. Cook, K. Anderson, Neutron Brillouin scattering in liquid <sup>36</sup>Ar, *Phys. B* 234–236 (1997) 308–310.
- [29] T. Pfleiderer, I. Waldner, H. Bertagnolli, K. Töoheide, B. Kirchner, H. Huber, H.E. Fischer, The structure of fluid argon from high-pressure neutron diffraction and ab initio molecular dynamics simulations, *J. Chem. Phys.* 111 (1999) 2641–2646.
- [30] J.M. Bomont, J.L. Bretonnet, T. Pfleiderer, H. Bertagnolli, Structural and thermodynamic description of supercritical argon with ab initio potentials, *J. Chem. Phys.* 113 (2000) 6815–6821.
- [31] B.M. Powell, H.F. Nieman, G. Dolling, Orientational disorder and diffuse scattering in β-nitrogen, *Chem. Phys. Lett.* 75 (1980) 148–151.
- [32] J.D. Sullivan, P.A. Egelstaff, The structure of nitrogen gas, *Mol. Phys.* 39 (1980) 329–342.
- [33] J.D. Sullivan, P.A. Egelstaff, The structure of nitrogen gas. II, *Mol. Phys.* 44 (1981) 287–297.
- [34] M. Deraman, J.C. Core, J.G. Powles, The structural second virial coefficient III. Nitrogen revisited, *Mol. Phys.* 52 (1984) 173–184.
- [35] P.S.Y. Cheung, J.G. Powles, The properties of liquid nitrogen, *Mol. Phys.* 32 (1976) 1383–1405.
- [36] P.A. Egelstaff, R.K. Hawkins, D. Litchinsky, P.A. de Lonngi, J.B. Suck, The structure and dynamics of dense nitrogen gas. I, *Mol. Phys.* 53 (1984) 389–396.
- [37] P.A. Egelstaff, G. Kearley, J.B. Suck, J.P.A. Youden, Neutron Brillouin scattering in dense nitrogen gas, *Europhys. Lett.* 10 (1989) 37–42.
- [38] J. Youden, P.A. Egelstaff, J. Mutka, J.B. Suck, The hydrodynamic limit for dense nitrogen and argon gases, *J. Phys. Condens. Matter* 4 (1992) 8945–8960.
- [39] P. Backx, P.A. Lonngi, P.A. Egelstaff, The structure and dynamics of dense nitrogen gas. II, *J. Phys. Condens. Matter* 5 (1993) 4265–4270.
- [40] J.J. Potoff, J.I. Siepmann, Vapor-liquid equilibria of mixtures containing alkanes, carbon dioxide, and nitroge, *AICHE J.* 47 (2001) 1676–1682.
- [41] P. Strąk, S. Krukowski, Molecular nitrogen-N<sub>2</sub> properties: the intermolecular potential and the equation of state, *J. Chem. Phys.* 126 (2007) 194501.
- [42] P. Strąk, S. Krukowski, The role of the intermolecular potential in determination of equilibrium and dynamic properties of molecular nitrogen (N<sub>2</sub>) properties: MD simulations, *J. Phys. Conf. Ser.* 121 (2008) 012011.
- [43] P. Strąk, S. Krukowski, Determination of shear viscosity of molecular nitrogen (N<sub>2</sub>): molecular dynamic hard rotor methodology and the results, *J. Phys. B* 115 (2011) 4359–4368.
- [44] C.R. Cioce, K. McLaughlin, J.L. Belof, B. Space, A polarizable and transferable PHAST N<sub>2</sub> potential for use in materials simulation, *J. Chem. Theory Comput.* 9 (2013) 5550–5557.
- [45] Phenomena Induced by Intermolecular Interactions, in: G. Birnbaum (Ed.), nATO ASI Series, vol. 127, Plenum, Boston, 1985.
- [46] J. Samios, U. Mittag, T. Dorfmueller, The far infrared absorption spectrum of liquid nitrogen, *Mol. Phys.* 56 (1985) 541–556.
- [47] <https://webbook.nist.gov/chemistry>, Accessed 23 August 2018.
- [48] I.W. Jones, J.S. Rowlinson, Gas-liquid critical temperatures of binary mixtures. Part 2, *Trans. Faraday Soc.* 59 (1963) 1702–1708.
- [49] J.S. Rowlinson, private communication, 2016.
- [50] A.K. Soper, D.T. Bowron, Density profile of nitrogen in cylindrical pores of MCM-41, *Chem. Phys. Lett.* 683 (2017) 529–535.
- [51] NIST Reference Fluid Thermodynamic and Transport Properties Database (REFPROP): Version 9.4.4.38 beta (2018), in: <https://trc.nist.gov/refprop/94/REFPROP.HTM>, 2018.
- [52] D.T. Bowron, A.K. Soper, K. Jones, S. Ansell, S. Birch, J. Norris, L. Perrott, D. Riedel, N.J. Rhodes, S.R. Wakefield, A. Botti, M.-A. Ricci, F.

- Grazzi, M. Zoppi, NIMROD: the Near and Intermediate Range Order Diffractometer of the ISIS second target station, *Rev. Sci. Instrum.* 81 (2010) 033905.
- [53] A.K. Soper, In: GudrunN and GudrunX: Programs for Correcting Raw Neutron and X-ray Diffraction Data to Differential Scattering Cross Section, Didcot, UK, 2011 <http://purl.org/net/epubs/work/56240>, Accessed 19 February 2015.
- [54] A.K. Soper, Partial structure factors from disordered materials diffraction data: an approach using empirical potential structure refinement, *Phys. Rev. B* 72 (2005) 104204.
- [55] A.K. Soper, Empirical Potential Structure Refinement - EPSRshell: a user's guide. Version 18 - May 2011, In: RAL Technical Report: RAL-TR-2011-012, 2011 <http://purl.org/net/epubs/manifestation/6709/RAL-TR-2011-012.pdf>.
- [56] J. Vrabc, J. Stoll, H. Hasse, A set of molecular models for symmetric quadrupolar fluids, *J. Phys. Chem. B* 105 (2001) 12126–12133.
- [57] T.B. Adler, G. Knizia, H. Werner, A simple and efficient CCSD(T)-F12 approximation, *J. Chem. Phys.* 127 (2007) 221106.
- [58] G. Knizia, T.B. Adler, H. Werner, Simplified CCSD(T)-F12 methods: theory and benchmarks, *J. Chem. Phys.* 130 (2009) 054104.
- [59] T.H. Dunning, Gaussian basis sets for use in correlated molecular calculations. I. The atoms boron through neon and hydrogen, *J. Chem. Phys.* 90 (1989) 1007–1023.
- [60] D.E. Woon, T.H. Dunning, Gaussian basis sets for use in correlated molecular calculations. III. The atoms aluminum through argon, *J. Chem. Phys.* 98 (1993) 1358–1371.
- [61] F. Weigend, A fully direct RI-HF algorithm: implementation, optimised auxiliary basis sets, demonstration of accuracy and efficiency, *Phys. Chem. Chem. Phys.* 4 (2002) 4285–4291.
- [62] F. Weigend, A. Köhn, C. Hättig, Efficient use of the correlation consistent basis sets in resolution of the identity MP2 calculations, *J. Chem. Phys.* 116 (2002) 3175–3183.
- [63] H.-J. Werner, P.J. Knowles, G. Knizia, F.R. Manby, M. Schütz, Molpro: a general - purpose quantum chemistry program package, *WIREs Comput. Mol. Sci.* 2 (2012) 242–253.
- [64] S.F. Boys, F. Bernardi, The calculation of small molecular interactions by the differences of separate total energies. Some procedures with reduced errors, *Mol. Phys.* 19 (1970) 553–566.
- [65] T.-S. Ho, H. Rabitz, A general method for constructing multidimensional molecular potential energy surfaces from ab initio calculations, *J. Chem. Phys.* 104 (1996) 2584–2597.
- [66] The HIBRIDON package (version 4.4) was written by M. H. Alexander, D. E. Manolopoulos, H.-J. Werner, B. Follmeg, and P. Dagdigian with contributions by D. Lemoine, P. F. Vohralik, G. Corey, R. Gordon, B. Johnson, T. Orlikowski, A. Berning, A. Degli-Esposti, C. Rist, B. Pouilly, J. Klos, Q. Ma, G. van der Sanden, M. Yang, F. de Weerd, S. Gregurick, and F. Lique, <http://www2.chem.umd.edu/groups/alexander>, 2017.
- [67] D.E. Manolopoulos, An improved log derivative method for inelastic scattering, *J. Chem. Phys.* 85 (1986) 6425–6429.
- [68] M.H. Alexander, D.E. Manolopoulos, A stable linear reference potential algorithm for solution of the quantum close-coupled equations in molecular scattering theory, *J. Chem. Phys.* 86 (1987) 2044–2050.
- [69] M.H. Alexander, Close-coupling studies of the orientation dependence of rotationally inelastic collisions, *J. Chem. Phys.* 67 (1977) 2703–2712.
- [70] D. Dellis, J. Samios, B. Collet, H. Versmold, J. Klos, S. Marinakis, An investigation of thermodynamics, microscopic structure, depolarized Rayleigh scattering, and collision dynamics in Xe-N<sub>2</sub> supercritical mixtures, *J. Mol. Liq.* 245 (2017) 42–51.
- [71] S. Marinakis, J. Samios, The temperature and density dependence of fluid xenon self-diffusion coefficients: a comparison between experimental, theoretical and molecular dynamics results, *J. Supercrit. Fluids* 34 (2005) 81–89.
- [72] I. Skarmoutsos, D. Dellis, J. Samios, Investigation of the local composition enhancement and related dynamics in supercritical CO<sub>2</sub> - cosolvent mixtures via computer simulation: the case of ethanol in CO<sub>2</sub>, *J. Chem. Phys.* 126 (2007) 224503.
- [73] I. Skarmoutsos, E. Guardia, J. Samios, Hydrogen bond, electron donor - acceptor dimer, and residence dynamics in supercritical CO<sub>2</sub> - ethanol mixtures and the effect of hydrogen bonding on single reorientational and translational dynamics: a molecular dynamics simulation study, *J. Chem. Phys.* 133 (2010) 014504.
- [74] I. Skarmoutsos, J. Samios, Local intermolecular structure and dynamics in binary supercritical solutions. A molecular dynamics simulation study of methane in carbon dioxide, *J. Mol. Liq.* 125 (2006) 181–186.
- [75] I. Skarmoutsos, S. Mossa, J. Samios, Structure and dynamics of liquid CS<sub>2</sub>: going from ambient to elevated pressure conditions, *J. Chem. Phys.* 145 (2016) 15405.
- [76] C.J. Eyles, M. Brouard, C.-H. Yang, J. Klos, F.J. Aoiz, A. Gijsbertsen, A.E. Wiskerke, S. Stolte, Interference structures in the differential cross-sections for inelastic scattering of NO by Ar, *Nat. Chem.* 3 (2011) 597–602.